Formation of stable aggregates by fluid-assembled solid bridges

Ali Seiphoori[a,b] ![ORCID], Xiao-guang Ma[c,d], Paulo E. Arratia[e], and Douglas J. Jerolmack[a,e,1] ![ORCID]

[a]Department of Earth & Environmental Science, University of Pennsylvania, Philadelphia, PA 19104; [b]Department of Earth, Atmospheric, & Planetary Sciences, Massachusetts Institute of Technology, Cambridge, MA 02139; [c]Department of Physics & Astronomy, University of Pennsylvania, Philadelphia, PA 19104; [d]Complex Assemblies of Soft Matter, Unité Mixte Internationale (UMI) 3254, CNRS-Solvay-University of Pennsylvania, Bristol, PA 19007; and [e]Department of Mechanical Engineering & Applied Mechanics, University of Pennsylvania, Philadelphia, PA 19104

When a colloidal suspension is dried, capillary pressure may overwhelm repulsive electrostatic forces, assembling aggregates that are out of thermal equilibrium. This poorly understood process confers cohesive strength to many geological and industrial materials. Here we observe evaporation-driven aggregation of natural and synthesized particulates, probe their stability under rewetting, and measure bonding strength using an atomic force microscope. Cohesion arises at a common length scale ($\sim$5 μm), where interparticle attractive forces exceed particle weight. In polydisperse mixtures, smaller particles condense within shrinking capillary bridges to build stabilizing "solid bridges" among larger grains. This dynamic repeats across scales, forming remarkably strong, hierarchical clusters, whose cohesion derives from grain size rather than mineralogy. These results may help toward understanding the strength and erodibility of natural soils, and other polydisperse particulates that experience transient hydrodynamic forces.

aggregate stability | evaporation | solid bridges | cohesion

Understanding the stability and strength of particle assemblies subject to disruptive forces is essential for predicting the macroscopic mechanical behavior of geological, biological, and industrial particulate materials (1–3). Hallmarks of such systems include size polydispersity and nonequilibrium dynamics (4, 5). In a polydisperse mixture, small particles may bind larger cohesionless grains together by bridging the interparticle space, forming aggregates. This mechanism is manifested in various industrial processes such as the flocculation of polymers (6, 7), cement binding of frictional grains (8, 9), contact fusion of metal particles during sintering (10, 11), and agglomeration of various industrial products, including commercial fertilizers and pharmaceutical products (12, 13). Various interfacial interactions—such as electrostatic and electromagnetic attractions (14), chemical bonding (15), capillary adhesion (16), solute (re)crystallization (17, 18), and nanoparticle–polymer interactions (19)—can confer strength to the particle assembly and give rise to an effective cohesion.

Evaporation of stable (electrostatically repulsive) colloidal suspensions can form aggregates (20–22), gels (23), and glasses (24), by driving particles together via capillary forces. In the absence of internal cohesive forces, however, the fluid-driven assembly should be unstable when subject to wetting or fluid shear. In the natural environment, soil cohesion determines the erosion susceptibility of landscapes, including riverbanks, marshes, hillsides, and agricultural fields (25–27). Cohesion is an important factor in geotechnical applications (28, 29), and a crucial parameter in transport of contaminants and microorganisms in the environment (30, 31). Many natural and industrial materials are composed of particles of various size, shape, and surface charge, and are subject to intermittent cycles of wetting and drying. The formation and mechanical stability of aggregates under these conditions has not been examined at the particle scale, and cannot be predicted from interfacial electrostatic forces.

Here we experimentally investigate the assembly of aggregates formed by evaporating various suspensions, and probe the stability of these aggregates subject to controlled rewetting (Fig. 1). We create an idealized model system composed of silica spheres of different sizes ranging from nanometer to micrometer scale, with well-characterized geometry and surface charge properties. We then compare results for a range of natural materials including clays (*Materials and Methods* and *SI Appendix*, Fig. S1). In each experiment, we first deposit a droplet of particle suspension on a borosilicate coverslip placed on an inverted optical microscope, and let it air dry under laboratory conditions (Fig. 1*A*). During evaporation, the suspended particles are subjected to both random and directional forces; the former includes Brownian and interparticle electrostatic forces (32), while the latter includes gravity and drag forces due to Marangoni flow (33) and an outward capillary flow [i.e., coffee ring flow (34)] that may pull suspended particles to the contact line as evaporation proceeds. During evaporation, the flow-induced forces (i.e., the outward convective flow and the capillary force at air–water interface) are dominant (34, 35). As evaporation proceeds, a contact line migrates inward in a stick–slip fashion due to partial pinning by defects on the surfaces of both the substrate and the substrate-bound particles. As a result, the suspended particles are either concentrated at a pinned edge or dragged toward the center by the retreating motion of the interface (Fig. 1*C*). Finally, the dried particles form unique patterns on the substrate as the result of a competition between the

Significance

Fine particles are light and reactive, leading them to aggregate under a range of conditions. Here we directly observe the particle-scale assembly of aggregates formed by evaporation, determine their stability during rewetting, and measure their interparticle bonding strength. Particles segregate by size due to capillary forces to form remarkable fractal structures. We discover that particle size, and not material properties, controls the cohesive strength of these aggregates, and we use physical principles to explain why. Results provide a view on the granular origins of cohesion that may improve our understanding of the mechanics of particulate materials with applications ranging from landslides to pharmaceuticals.
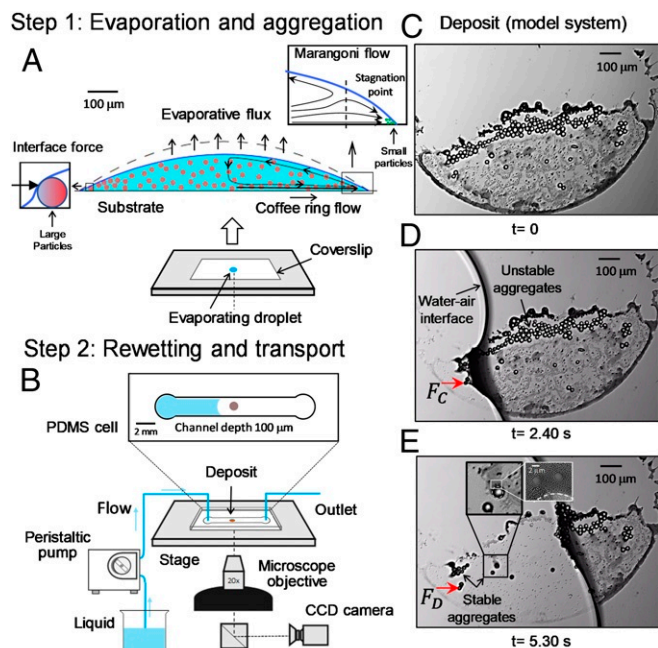
Fig. 1. Approach for examining experimental assembly and stability of aggregates. (*A* and *B*) Experimental design. CCD, charged coupled device. (*C*) Evaporation pattern of a polydisperse system composed of silica spheres. (*D*) Transport mechanism due to a transient capillary interface (contact line) migrating across the channel, imposing a capillary force on particles, F_C. (*E*) Transport mechanism due to a laminar flow regime, imposing a drag force on particles, F_D.

flow-induced forces and the colloid–substrate interaction during evaporation (36, 37).

After evaporation, we fully dry the particle deposits by applying a vacuum, and image sample aggregates using Scanning and Transmission Electron Microscopes (SEM and TEM) to obtain the fine details of their structure. We subsequently mount a microfluidic channel onto the coverslip over the aggregates (Fig. 1*B* and *Materials and Methods*). A pump then flows water through the channel and over the aggregate, where rewetting occurs in three steps: First, the increase in humidity in the channel induces water condensation on surfaces of both the substrate and the particles; second, a transient capillary interface (contact line) migrates across the channel; and, third, a steady (fully saturated) laminar flow develops and applies fluid shear to the aggregates (Fig. 1 *D* and *E*). We note that the capillary force imposed by the moving contact line depends on the wetting properties of the particle surfaces. For partially wetted surfaces (as shown in the model system presented in Fig. 1*D*), the contact line deforms due to pinning by particles. The resultant capillary force is orders of magnitude larger than the drag and lift forces imparted on the particles by the saturated flow (*SI Appendix*, section 1 and Fig. S2). As a result, particle entrainment typically occurs by the moving contact line; most aggregates remaining can withstand the subsequent hydrodynamic forces after inundation (Movie S1).

Formation of Stabilizing Solid Bridges

We first examine the drying and rewetting dynamics of a suspension of bidisperse silica microspheres composed of 20-μm and 3-μm particles with concentration of 2.0 and 0.2 wt %, respectively. We note that the surfaces of the silica particles and the coverslip are all negatively charged in water. Thus particle–particle and particle–substrate interactions in suspension are expected to be repulsive (*SI Appendix*, Fig. S1). In addition, we

pretreat the coverslip to make it more hydrophilic to encourage the formation of widely dispersed, isolated aggregates (rather than one large aggregate as seen in Fig. 1*C*; see *Materials and Methods*). As evaporation of the droplet begins, the retreating air–water interface drags smaller particles and condenses some of them within the meniscus formed between larger particles and the substrate or between adjacent particles (Fig. 2 *A–C* and Movie S2). Once all water is evaporated, we find that these small particles form "solid bridges" that connect larger particles to the substrate and to each other to form aggregates (Fig. 2*C*). The deposit is then subject to rewetting by a transient capillary flow with an average velocity $u = 180$ μm/s and Reynolds number $\Re = 0.03$ (Fig. 2 *D–F*). We find that the 20-μm particles that are stabilized through solid bridging are not transported by the flow (Movie S3). In contrast, evaporating a monodisperse suspension of 20-μm particles generates a deposit without solid bridges that is easily resuspended and transported by the flow (Fig. 2 *G–I* and Movie S4). Our results show that particles roughly 5 μm and smaller form stable aggregates when dried from a monodisperse suspension. These small particles are not only stable; when present, they also tend to stabilize larger particles by bridging interparticle space, binding large particles to one another and also to the substrate.

Hierarchical Structure of Aggregates

We observe a consistent and intriguing pattern in the aggregates formed from the bidisperse suspension: Small particles surround larger ones in a concentric arrangement. It appears that, as the droplet evaporates, it breaks up into smaller regions around the larger particles; the retreating contact line then drags small particles radially inward toward each large particle (Fig. 2*C*). To further probe this pattern-forming process, we
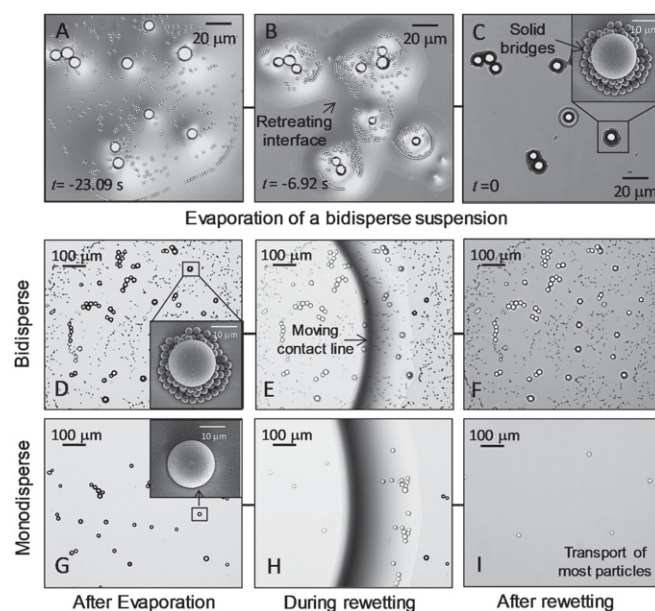

Fig. 2. Contribution of solid bridges to stabilizing the evaporation-induced aggregates. (*A* and *B*) Evaporation from a bidisperse suspension composed of 20- and 3-μm silica spheres, where smaller particles condense within the diminishing capillary bridges. (*C*) Formation of solid bridges between larger particles or between particles and the substrate. A higher magnification of an aggregate formed by solid bridges is presented in the *Inset*. (*D–F*) Stability of aggregates due to the presence of solid bridges. An isolated aggregate is shown in the *Inset* of photomicrograph *D* under higher magnification. (*G–I*) Transport of 20-μm particles in the absence of smaller particles and the associated solid bridges. An isolated particle is shown in the *Inset* of photomicrograph *G* under higher magnification.
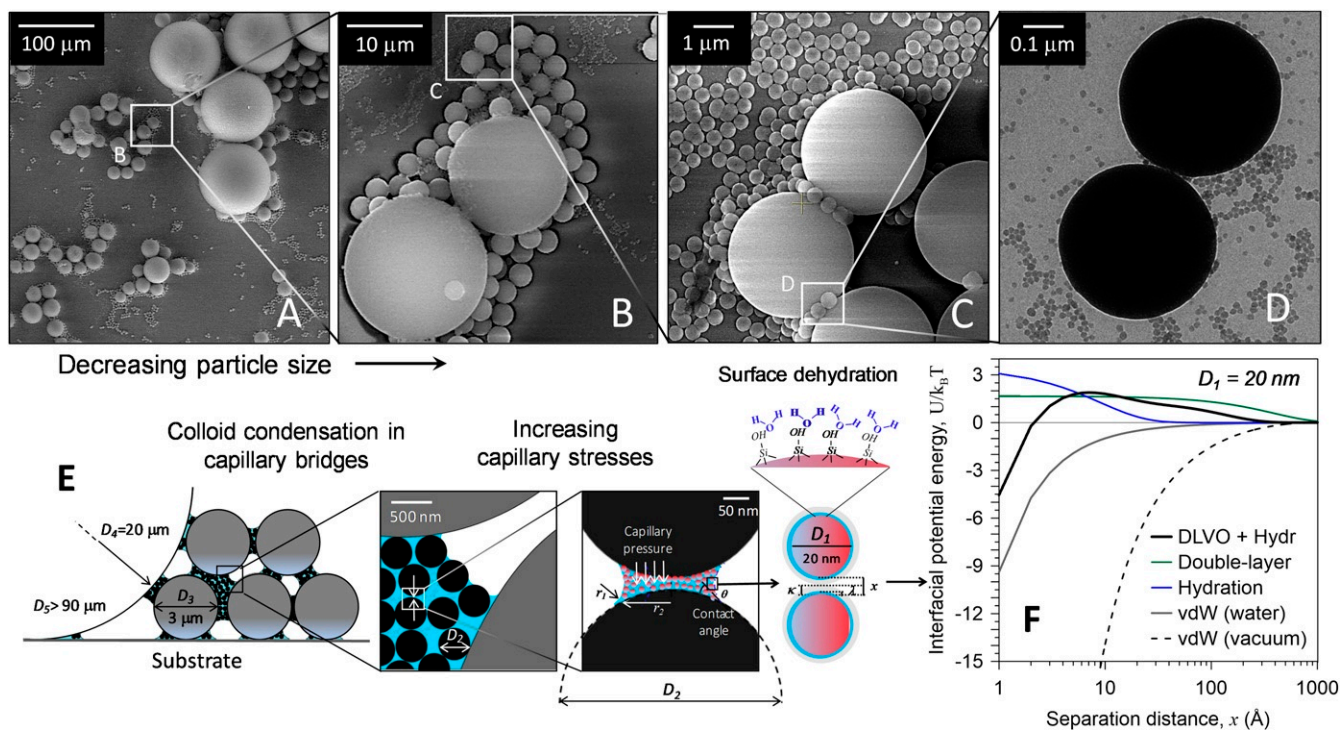
Fig. 3. Hierarchical structure of aggregates. (*A–D*) Multiscale observation of a polydisperse colloidal system composed of silica spheres with particle sizes of 90, 20, 3, and 0.4 μm along with silica nanoparticles of 20-nm size. (*E*) Capillary force drives particles together by overcoming the interparticle repulsion. Further dehydration of the particle surface is energetically favorable, resulting in an overall van der Waals (vdW) attraction between particles. (*F*) Interfacial potential energy functions between two particles of D_1 = 20-nm size, calculated from theory (*SI Appendix*, section 2).

examine the evaporation of a polydisperse suspension composed of five different particle sizes: 90, 20, 3, 0.4, and 0.02 μm at 5.0, 2.0, 0.2, 0.01, and 0.001 wt %, respectively (Fig. 3 *A–D*). A multiscale observation of the deposited aggregates reveals a remarkable self-similar, hierarchical structure of particle aggregates formed by solid bridges. The resulting aggregates are strongly size-segregated, with large particles ringed by smaller particles, and those particles ringed by even smaller particles, and so on. Although classical aggregation is known to make fractal structures (38–40), this hierarchical arrangement of particle sizes seems to be a special consequence of evaporation-induced aggregation. Evaporation and breakup of the droplet drives the cascading assembly of aggregates from large to small pore spaces via capillary pressure, which condenses smaller colloids within the capillary bridges at each scale (Fig. 3*E*). We note that the aggregates formed by polydisperse silica spheres are stable when subject to rewetting.

We now consider the relevant physical parameters that allow the assembly and stability of aggregates formed by evaporation. We begin by calculating the pair-wise potential energy between particles by incorporating double-layer repulsion and van der Waals attraction potentials (as in Derjaguin-Landau-Verwey-Overbeek [DLVO] theory), as well as the surface hydration potential (*SI Appendix*, section 2). We estimate energy as a function of the surface-to-surface distance, x, between, for instance, two approaching D_1 = 20-nm silica particles in water during evaporation (Fig. 3*F*), where D_1 is the smallest particle size in the model system (Fig. 3). We find that the maximum energy of the capillary bridge between these particles under evaporation ($\gamma D_1^2 \approx 10^3\ k_B T$) is much larger than the repulsive barrier, and should easily push particles within the range of van der Waals attraction (41, 42). Furthermore, full dehydration of the surfaces (e.g., by applying vacuum as in our experiments) further enhances the van der Waals attraction (Fig. 3*F*). The 20-nm

particles condense within the capillary bridges among the next-largest particle of D_2 = 400 nm (Fig. 3*D*), and the 400-nm particles condense within the capillary bridges of 3 μm (Fig. 3*C*), and so on. We note that our distinct size classes of silica particles here are about an order of magnitude different. Our TEM images, however, show that unintentional amorphous silica nanoparticles—close in size to the 2-nm resolution limit of our images—also form solid bridges (*SI Appendix*, Fig. S4). This may suggest that the solid bridging effect plays out down to very small length scales, but we are unsure what the lower limit for this capillary drying effect is. We note that size segregation of polydisperse nanoparticles (1.5 to 6 nm diameter) has been previously reported, and attributed to a different mechanism: size-dependent dispersion interactions (43). This effect becomes less relevant for larger particles; while it may have contributed to aggregation for our smallest 2-nm silica contaminants, it is unlikely to be relevant for the ≥20-nm particles we focus on here. Accordingly, it seems reasonable that evaporation creates a multiscale aggregate system with strong interparticle bonds, by collecting small particles around the contact points of larger particles.

Solid Bridging in Naturally Occurring Particles

To further test the generality of stabilization by solid bridging, we investigate suspensions of two structurally distinct, naturally occurring clay types: illite, the most common clay mineral with a 2:1 (TOT phyllosilicate) structure; and kaolinite, a widely used industrial clay with a simple 1:1 (TO phyllosilicate) structure (44). Despite having more complex shapes and surface charge properties (*SI Appendix*, Fig. S1), we identify a behavior in clay particles similar to that of the idealized silica spheres. Consider a polydisperse suspension of illite particles ranging from 0.1 μm < d < 100 μm. We find that evaporation forms solid bridges and strong aggregates that are stable in reaction to rewetting
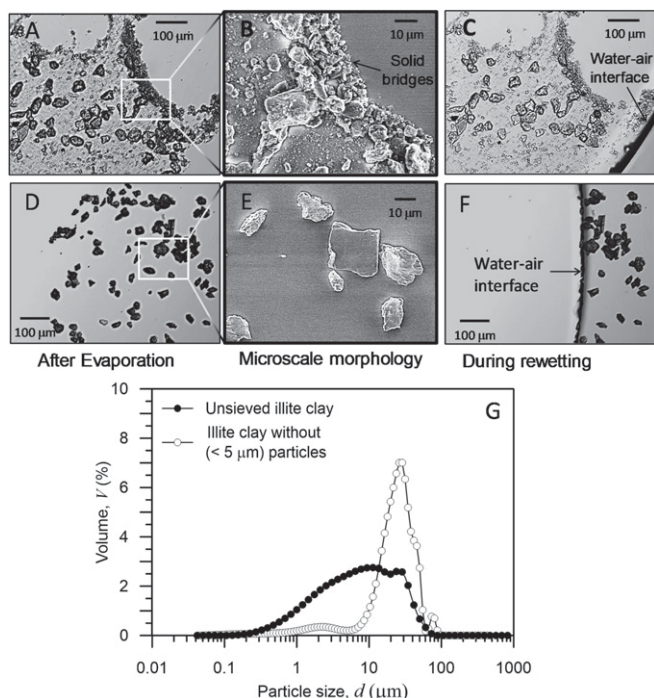
APPLIED PHYSICAL SCIENCES

Fig. 4. Stability of aggregates of illite clay particles through formation of solid bridges. (*A*) Aggregates formed by unsieved, polydisperse illite particles. (*B*) Morphology of the solid bridges at microscopic scale. (*C*) Aggregates are stable when subject to rewetting, due to solid bridges. (*D*) Aggregates of same illite clay modified by sieving out particles of <5 μm. (*E*) Morphology of illite particle deposits. (*F*) Removal of small particles makes aggregates unstable in reaction to rewetting. (*G*) Particle size distributions of unsieved and sieved illite particle suspensions.

(Fig. 4 *A–C* and Movie S5). Sieving the illite clay to remove particles with $d < 5$ μm, however, leads to aggregates that disintegrate when rewetted (Fig. 4 *D–F* and Movie S6), suggesting that smaller particles are critical for solid bridge formation. Kaolinite clay particles exhibit similar behavior to illite (Movies S7 and S8). These results demonstrate that solid bridging induces an effective cohesion in polydisperse aggregates, and that this effect is insensitive to material properties. We note that it is difficult to discern a hierarchical structure for unsieved illite clay aggregates, possibly due to the continuous size distribution (Fig. 4*G*). To facilitate direct comparison with the silica spheres, we modified the size distribution of illite particles with four selected size classes of approximately one order of magnitude difference. We observe a clear expression of hierarchical multiscale aggregation due to evaporation (*SI Appendix*, Fig. S3). Despite the anisotropic shapes and nonuniform surface charge distributions of these natural clay particles, they reproduce the general behavior seen in the idealized case of polydisperse silica spheres.

Strength Conferred by Solid Bridges

The stability of aggregates formed by evaporation depends on two factors: 1) the strength of interparticle bonds within the aggregates and 2) the "anchoring" force between the aggregates and the substrate. For a deposit to resist the flow during rewetting, both bonds need to be strong. To quantify the interparticle strength due to bonds formed by solid bridges, we use an atomic force microscope (AFM) to determine the detachment (pull-off) force and energy associated with 20-μm silica spheres (Fig. 5 and *Materials and Methods*). We first deposit a monodisperse suspension of 20-μm particles on a coverslip, where solid bridging is not expected. Images indicate, however, that nanopar-

ticulate contamination composed of amorphous silica is nearly unavoidable; this is expected to confer some strength to the particles (*SI Appendix*, Fig. S4). The AFM force–displacement curves ($F_s - z$) initially have a positive force associated with the compression of the cantilever onto the particle (Fig. 5); as the cantilever is lifted, F_s grows increasingly negative, until detachment occurs and it abruptly drops to zero. The maximum (pull-off) force measured using this technique for the 20-μm particles in monodisperse systems is of order 10^{-8} N. The energy associated with detaching the 20-μm particle from the substrate is characterized as the total area between the zero deflection line and the force–displacement curve; it is of order $10^5 \, k_B T$ (Fig. 5 *A*, *Inset*). This is much larger than the measured adhesion force between the particle and the substrate after detachment (see *Materials and Methods*). The measured value is consistent with an estimate from the van der Waals interaction of a sphere with diameter $D = 20$ μm and a flat substrate ($-AD/12x \approx -2.6 \times 10^5 \, k_B T$, $x = 0.1$ nm), which suggests that this cohesive force could be roughly estimated for other materials and systems (*SI Appendix*, section 2).

To examine the additional strength conferred by solid bridges, compared to the monodisperse case, we perform similar detachment experiments on 20-μm particles deposited from bidisperse (20 and 3 μm) and polydisperse (20, 3, 0.4, and 0.02 μm) suspensions. The force–displacement curve in these cases displays multiple stick–slip events (Fig. 5*A*), which are likely due to the breaking of individual or groups of bonds associated with solid bridges. This mechanism increases the detachment energy of the 20-μm particles in bidisperse and polydisperse systems by ∼15 and 20 times, respectively (Fig. 5 *A*, *Inset*). Detailed SEM images (*SI Appendix*, Fig. S5) suggest that the 20-μm particles in these deposits are supported by a finite number of contacts
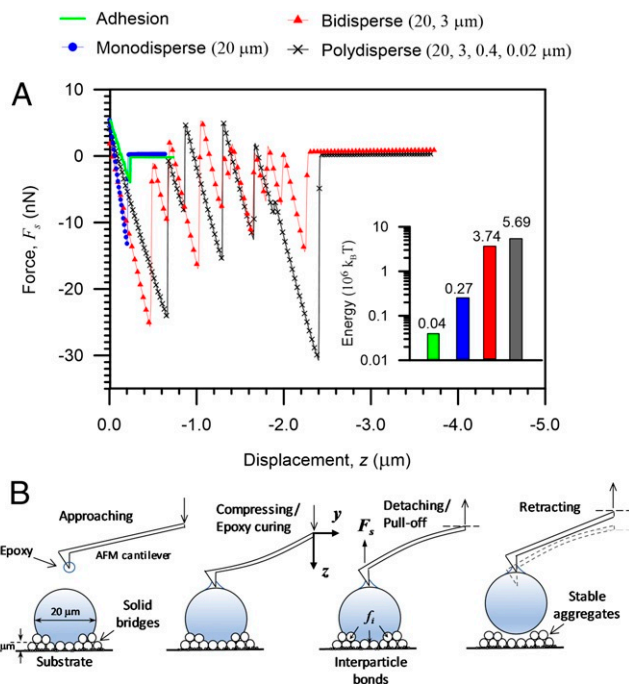

Fig. 5. Pull-off force measured with AFM using contact mode technique. (*A*) Force–displacement ($F_s - z$) and detachment energy (*Inset*) of a single 20-μm silica particle after evaporation from monodisperse, bidisperse, and polydisperse suspensions. The adhesion force between the 20-μm particle and the substrate is also shown for reference. (*B*) Modifying the AFM contact mode procedure for pull-off experiments. In the presence of solid bridges, F_s is associated with breaking of individual bonds or groups of bonds at the contact points (f_i) with the underlying structure formed by smaller particles.

Seiphoori et al.

with the underlying structures formed by smaller particles ($\leq 3\mu m$). For instance, in the bidisperse case here, the number of contacts would be roughly $n \approx 30$ (*SI Appendix*, Fig. S5*D*). We assume that the total detachment energy of the larger particle ($D = 20$ μm) is associated with the sum of all individual bonds with smaller particles ($D' = 3$ μm), plus a single bond with the substrate. The total van der Waals energy estimated for this configuration is $\sim -n[(A/12x)(DD'/(D + D'))] - AD/12x \approx -1.3 \times 10^6 \, k_B T$ ($x = 0.1$ nm), which is consistent with our AFM detachment experiment. We find that, after detaching the 20-μm particles, the underlying deposits of smaller particles remain stable in reaction to subsequent rewetting (*SI Appendix*, Fig. S5 *H and I*). This reinforces the notion that the bonding mechanism described here for evaporation-driven suspensions is relevant for particles smaller than ~ 5 μm. We note that the measured detachment forces and energies using the AFM may not be reflective of conditions associated with detachment by water; hydration due to humidity precedes the wetting front (Movie S9), and could weaken interparticle bonds (45) relative to the conditions of the AFM. Nevertheless, AFM results provide a useful relative measure of the stability conferred on large particles by solid bridging of smaller particles.

Discussion

We have examined the particle-scale assembly of aggregates formed by evaporation, and probed their mechanical stability under subsequent rewetting and fluid shear. While surface properties such as charge type and density influence particle interactions in suspension, our results show how interfacial capillary force can dominate over electrostatic effects. During evaporation, particles tend to be concentrated at the contact points, where attractive bonds develop. Those individual bonds may be weak (e.g., short-range van der Waals type), but the sum of attractive forces and the resultant cohesion can be remarkably large, especially for systems with a large number of contacts. Such behavior is facilitated by the presence of small particles that effectively increase the specific surface area of the system. True cohesion in natural soils is typically attributed to the presence of clay minerals, or other cementing agents such as carbonates, iron oxides, and salts (44, 46). We have shown that a typical clay material effectively loses its cohesion when small particles are absent, while silica particles (≤ 5 μm) with simple interparticle contact properties form cohesive aggregates (*SI Appendix*, Figs. S5 and S6). Indeed, for a range of materials, we observe a transition from cohesionless to cohesive aggregates at a common length scale, where interparticle forces exceed the particle weight (*SI Appendix*, Fig. S6). Thus, attributing the cohesion in natural soils to material properties (e.g., by introduction of clay minerals) might obscure the contribution made by the particle size. Soils are composed of polydisperse particles subject to cycles of evaporation and rewetting. It is possible that the formation and strength of soil aggregates has more to do with size than with material composition. The wetting behavior of soils is of fundamental importance for soil collapse (47, 48), creep and liquefaction in landslides (28, 49), and slaking erosion that results from disintegration of aggregates (27, 29). Modeling frameworks consider only granular friction, fluid drag, and pore pressure effects. Our findings reveal a mechanism of fluid–particle interaction that governs soil strength, and suggest that stability of loose soils may be enhanced by addition of nanoparticles (*SI Appendix*, Fig. S7). Determining the onset and consequences of cohesion may also aid industrial applications, where granular materials handling relies on understanding and exploiting rheology (50). More broadly, our results open the path to studying the effect of particle size polydispersity and transient hydrodynamic forces on the multiscale mechanical behavior of particulate assemblies ranging from industrial to complex living systems. In addition, hierarchical assembly of aggregates by evaporation may provide a novel method for creating thin films with desired mechanical properties (51, 52).

Materials and Methods

Particle Properties and Preparation of Suspensions. Various silicate-based colloids were selected to encompass a wide range of relative charge, shape, and size heterogeneity. Aqueous suspensions of silica microspheres (Corpuscular Inc.) with mean diameter of 20, 3, 0.4, and 0.02 μm (particle density, ρ_s = 2.65 g/cm^3) were diluted in deionized water (Milli-Q Reagent Water System; Millipore) and mixed to form an idealized polydisperse model system. Mined phyllosilicate clay minerals including illite (pulverized Cambrian shale from Silver Hill formation) and kaolinite (Washington County formation, Georgia) were used to represent natural soil particles. The particle density of illite and kaolinite was measured as ρ_i = 2.77 g/cm^3 and ρ_k = 2.65 g/cm^3, respectively. The BET (Brunauer, Emmett, and Teller) surface area of the illite and kaolinite particles was measured as 10.98 m^2/g, and 9.09 m^2/g using a Micromeritics 3Flex surface area analyzer (Micromeritics Instrument Co.). Dry clay particles were initially dispersed in deionized water and allowed to rest for 24 h. The suspension was then sonicated and passed through a 90-μm sieve (No. 170 ASTM-E11; American Society for Testing and Materials [ASTM]) to filter out large aggregates. The particle size distribution of the clay suspension was computed using a laser diffraction analyzer equipped with an ultrasonic dispersing module (Beckman Coulter, Inc.). To produce a monodisperse clay suspension, small particles (<5 μm) were removed through multiple wet sieving (5-μm mesh screen [316L], Utah Biodiesel Supply) and ultrasonic washing of the particles submerged in deionized water. After each attempt, the particle size distribution of the suspension was measured, and samples were examined using an optical microscope to ensure the elimination of small particles. The electrophoretic mobility of the colloidal suspension of silica microspheres (3-μm size) and clay particles (size of <5 μm) were measured at various pH values using a ZetaPALS instrument (Brookhaven), on 15 to 20 parts per million particle suspensions at temperature $25.0 \pm 0.5 °C$. The pH values were adjusted by dropwise addition of HCl or KOH solutions. Given the polydispersity of the shape and size of the clay particles, the zeta potentials were estimated using the Helmholtz–Smoluchowski equation (53). The average zeta potential of silica spheres, illite particles, and kaolinite particles were measured as −54.9, −27.7, and −32.6 mV for pH = 7.0 ± 0.5, where the evaporation and rewetting experiments were conducted.

Evaporation and Rewetting Experiments. The colloidal droplets ($\sim$0.1 μL) were initially placed on a borosilicate glass coverslip (Fisher Scientific; thickness varying from 0.13 to 0.17 mm). The droplet was then air dried due to evaporation under laboratory conditions (relative humidity [RH] = 0.50 ± 0.05, $T = 22 °C$). The coverslip glass has an average root-mean-square roughness of 1.3 ± 0.35 nm as measured by AFM technique (Icon; Bruker Co.). Precleaning the coverslip by dipping in acetone for 5 min, rinsing with isopropyl alcohol and deionized water, and then drying using compressed nitrogen gas resulted in a semihydrophilic surface (contact angle $30.0 \pm 2.5°$) that tended to lead to clumped aggregates (as in Fig. 1). To encourage the formation of widely dispersed, isolated aggregates after evaporation, the coverslip surface was pretreated by using O$_2$ plasma (SCE-108 Barrel Asher; Anatech USA) under a radio frequency power of 50 W for a duration of 15 s under chamber pressure of 300 mTorr. This treatment provides a more hydrophilic surface with a small contact angle for the water film on the glass (contact angle $8.0 \pm 2.5°$). By creating isolated aggregates, we were able to perform AFM pull-off experiments on a single 20-μm particle bound to the substrate through solid bridges formed by smaller particles. The deposit was then placed in a vacuum chamber (500 mTorr), and, after another O$_2$ plasma treatment (50 W for 15 s), a microfluidic device was mounted on the coverslip so that the deposit was aligned within a rectangular channel with dimensions of 100 μm height, 2 mm width, and 20 mm length. The microfluidic device was made of polydimethylsiloxane (PDMS) using standard soft-lithography methods (54). The fluid was pumped through the channel via a positive displacement peristaltic pump (Minipuls 3; Gilson) under a nonslip boundary condition. The channel was then subject to a rehydration path through a steady and laminar flow.

Multiscale Observation. The microfluidic device was positioned on an inverted microscope, Elipse Ti-E, (Nikon Instrument Inc.), with a 20x objective (numerical aperture [N.A.] = 0.75, resolution = 0.37 μm), where the images were acquired using an Andor iXon3 EMCCD camera by NIS Elements software (Nikon Instrument Inc.). SEM images were acquired using an environmental SEM, FEI Quanta 600 FEG (Thermo Fisher Scientific) operating at

APPLIED PHYSICAL SCIENCES

10 to 30 keV equipped with an electron backscatter diffraction analyzer to provide the energy-dispersive X-ray spectroscopy for chemical phase analysis. TEM images were acquired using a field emission scanning TEM (Japan Electron Optics Laboratory [JEOL] Ltd., F200), operating at 120 keV. Selected area (electron) diffraction (SAED) technique was employed to obtain information on the crystal structure of the solid bridges.

AFM Measurements. The detachment (pull-off) force was measured by modifying the contact mode of an AFM Asylum MFP-3D unit (Asylum Research) mounted on top of the same inverted microscope system (Elipse Ti-E), and the force spectroscopy data were obtained using the IGOR PRO program (WaveMetrics). Soft contact-mode cantilevers made of silicon nitride (NanoAndMore Co.), 250 to 350 μm long with spring constant of 0.03 to 0.08 N/m, and Al backside coating, were used to cover the range of measured forces. To minimize the effect of adhesion due to humidity, all samples were subjected to vacuum (500 mTorr) prior to AFM detachment experiments. Increasing the relative humidity is expected to increase the capillary adhesion and thus the AFM detachment force (16). The exact spring constant value of each cantilever was determined using the thermal calibration method prior to detachment experiment. Devcon 5-Minute Epoxy (Devcon Co.) was then prepared according to the manufacturer's instructions directly on a coverslip strip and flattened to form a thin film. The apex of the cantilever was approached to the film until contact with the epoxy surface was observed. The cantilever was then pulled up immediately to prevent an excessive amount of epoxy due to capillary action. After depositing a small bead of epoxy, the apex of the cantilever was moved on top and pushed onto the target particle. The epoxy was then allowed to cure for 15 min and solidify. The experiment was performed by lifting the cantilever, while deflection data were recorded. The scan rate (loading/unloading rate) was 0.50 Hz in all experiments. The set point, or zero deflection position, in the noncontact regime was set to the zero-voltage position for all force curves. Following the detachment of a single 20-μm particle from the substrate in a monodisperse system, we corrected the cantilever stiffness using thermal calibration data and measured the adhesion force between the particle and the substrate with values found in the range of 4 ± 2 nN for several spots on the substrate. The adhesion force between the bare AFM apex and the 20-μm particles surface was measured to be in the range of 2 ± 1 nN. The total detachment energy was characterized as the total area between the zero deflection line and the force–displacement curve from the point where the line crosses zero to the final jump back up to zero. The AFM measurements were carried out in the quasi-static regime, where the force curve should be completely determined by the elastic modulus of the cantilever. The thermal calibration we performed indicated a dissipation factor in the range of 2.1 to 3.2%, confirming that dissipation was negligible compared to measured forces.

Data Availability. Details for the calculation of the hydrodynamic forces acting on particles during rewetting and the interfacial potential energy of approaching colloidal particles are provided in *SI Appendix*, sections 1 and 2, respectively. Movies S1–S10, related to this study, are also publicly available at https://github.com/seiphoori/FSSB.

1. F. Chiti, M. Stefani, N. Taddei, G. Ramponi, C. M. Dobson, Rationalization of the effects of mutations on peptide and protein aggregation rates. *Nature* **424**, 805–808 (2003).
2. S. B. Mueller *et al.*, Stability of volcanic ash aggregates and break-up processes. *Sci. Rep.* **7**, 7440 (2017).
3. H. Zhang *et al.*, Stable colloids in molten inorganic salts. *Nature* **542**, 328–331 (2017).
4. V. J. Anderson, H. N. W. Lekkerkerker, Insights into phase transition kinetics from colloid science. *Nature* **416**, 811–815 (2002).
5. Y. Xia *et al.*, Self-assembly of self-limiting monodisperse supraparticles from polydisperse nanoparticles. *Nat. Nanotechnol.* **6**, 580–587 (2011).
6. J. Swenson, M. V. Smalley, H. L. M. Hatharasinghe, Mechanism and strength of polymer bridging flocculation. *Phys. Rev. Lett.* **81**, 5840–5843 (1998).
7. S. Biggs, M. Habgood, G. J. Jameson, Y.-d. Yan, Aggregate structures formed via a bridging flocculation mechanism. *Chem. Eng. J.* **80**, 13–22 (2000).
8. P. C. Fonseca, H. M. Jennings, The effect of drying on early-age morphology of C–S–H as observed in environmental SEM. *Cement Concr. Res.* **40**, 1673–1680 (2010).
9. T. Zhou, K. Ioannidou, F.-J. Ulm, M. Z. Bazant, R. J.-M. Pellenq, Multiscale poromechanics of wet cement paste. *Proc. Natl. Acad. Sci. U.S.A.* **116**, 10652–10657 (2019).
10. S. E. Wanke, P. C. Flynn, The sintering of supported metal catalysts. *Catal. Rev.* **12**, 93–135 (1975).
11. F.W. Dynys, J. W. Halloran, Influence of aggregates on sintering. *J. Am. Ceram. Soc.* **67**, 596–601 (1984).
12. D. Bika, G. I. Tardos, S. Panmai, L. Farber, J. Michaels, Strength and morphology of solid bridges in dry granules of pharmaceutical powders. *Powder Technol.* **150**, 104–116 (2005).
13. C. Avilés-Avilés, E. Dumoulin, C. Turchiuli, Fluidised bed agglomeration of particles with different glass transition temperatures. *Powder Technol.* **270**, 445–452 (2015).
14. P. J. Lu *et al.*, Gelation of particles with short-range attraction. *Nature* **453**, 499–503 (2008).
15. D. M. Roy, New strong cement materials: Chemically bonded ceramics. *Science* **235**, 651–658 (1987).
16. R. Jones, H. M. Pollock, J. A. S. Cleaver, C. S. Hodges, Adhesion forces between glass and silicon surfaces in air studied by AFM: Effects of relative humidity, particle size, roughness, and surface treatment. *Langmuir* **18**, 8045–8055 (2002).
17. F. Soulié, M. S. El Youssoufi, J.-Y. Delenne, C. Voivret, C. Saix, Effect of the crystallization of a solute on the cohesion in granular materials. *Powder Technol.* **175**, 43–47 (2007).
18. R. Guo, T. Hueckel, Growth of polymer microstructures between stressed silica grains: A chemo-mechanical coupling. *Geotechnique* **63**, 322–330 (2013).
19. S. Rose *et al.*, Nanoparticle solutions as adhesives for gels and biological tissues. *Nature* **505**, 382–385 (2014).
20. M. Liu, B. Guo, M. Du, D. Jia, Drying induced aggregation of halloysite nanotubes in polyvinyl alcohol/halloysite nanotubes solution and its effect on properties of composite film. *Appl. Phys. A* **88**, 391–395 (2007).
21. V. N. Manoharan, M. T. Elsesser, D. J. Pine, Dense packing and symmetry in small clusters of microspheres. *Science* **301**, 483–487 (2003).
22. A. Thill, O. Spalla, Aggregation due to capillary forces during drying of particle submonolayers. *Colloid. Surf. Physicochem. Eng. Asp.* **217**, 143–151 (2003).
23. L. Pauchard, F. Parisse, C. Allain, Influence of salt content on crack patterns formed through colloidal suspension desiccation. *Phys. Rev. E* **59**, 3737–3740 (1999).
24. M. D. Haw, M. Gillie, W. C. K. Poon, Effects of phase behavior on the drying of colloidal suspensions. *Langmuir* **18**, 1626–1633 (2002).
25. I. J. Smalley, Cohesion of soil particles and the intrinsic resistance of simple soil systems to wind erosion. *J. Soil Sci.* **21**, 154–161 (1970).
26. A. D. Howard, C. F. McLane III, Erosion of cohesionless sediment by groundwater seepage. *Water Resour. Res.* **24**, 1659–1674 (1988).
27. B. Barthes, E. Roose, Aggregate stability as an indicator of soil susceptibility to runoff and erosion; validation at several levels. *Catena* **47**, 133–149 (2002).
28. K. Ishihara, Liquefaction and flow failure during earthquakes. *Geotechnique* **43**, 351–451 (1993).
29. M. Li *et al.*, Modelling soil detachment by overland flow for the soil in the Tibet plateau of China. *Sci. Rep.* **9**, 8063 (2019).
30. J. McCarthy, J. Zachara, Subsurface transport of contaminants. *Environ. Sci. Technol.* **23**, 496–502 (1989).
31. T. R. Garrett, M. Bhakoo, Z. Zhang, Bacterial adhesion and biofilms on surfaces. *Prog. Nat. Sci.* **18**, 1049–1056 (2008).
32. C. Allain, L. Limat, Regular patterns of cracks formed by directional drying of a collodial suspension. *Phys. Rev. Lett.* **74**, 2981–2984 (1995).
33. M. Maillard, L. Motte, A. T. Ngo, M. P. Pileni, Rings and hexagons made of nanocrystals: A Marangoni effect. *J. Phys. Chem. B* **104**, 11871–11877 (2000).
34. R. D. Deegan *et al.*, Capillary flow as the cause of ring stains from dried liquid drops. *Nature* **389**, 827–829 (1997).
35. B. M. Weon, J. H. Je, Capillary force repels coffee-ring effect. *Phys. Rev. E* **82**, 015305 (2010).
36. G. D. Nadkarni, S. Garoff, An investigation of microscopic aspects of contact angle hysteresis: Pinning of the contact line on a single defect. *Europhys. Lett.* **20**, 523–528 (1992).
37. R. D. Deegan, Pattern formation in drying drops. *Phys. Rev. E* **61**, 475–485 (2000).
38. D. W. Schaefer, J. E. Martin, P. Wiltzius, D. S. Cannell, Fractal geometry of colloidal aggregates. *Phys. Rev. Lett.* **52**, 2371–2374 (1984).
39. M. Y. Lin *et al.*, Universality in colloid aggregation. *Nature* **339**, 360–362 (1989).
40. C. Kranenburg, The fractal structure of cohesive sediment aggregates. *Estuar. Coast Shelf Sci.* **39**, 451–460 (1994).
41. J. N. Israelachvili, *Intermolecular and Surface Forces* (Academic, ed. 3, 2015).

42. Y. I. Rabinovich, M. S. Esayanur, B. M. Moudgil, Capillary forces between two spheres with a fixed volume liquid bridge: Theory and experiment. *Langmuir* **21**, 10992–10997 (2005).
43. P. C. Ohara, D. V. Leff, J. R. Heath, W. M. Gelbart, Crystallization of opals from polydisperse nanoparticles. *Phys. Rev. Lett.* **75**, 3466–3469 (1995).
44. J. K. Mitchell, K. Soga, *Fundamentals of Soil Behavior* (Wiley, Hoboken, NJ, ed. 3, 2005).
45. J. Israelachvili, H. Wennerström, Role of hydration and water structure in biological and colloidal interactions. *Nature* **379**, 219–225 (1996).
46. J. C. Winterwerp, W. G. M. Van Kesteren, *Introduction to the Physics of Cohesive Sediment Dynamics in the Marine Environment* (Elsevier, ed. 3, 2004), vol. 56.
47. L. Barden, A. McGown, K. Collins, The collapse mechanism in partly saturated soil. *Eng. Geol.* **7**, 49–60 (1973).
48. I. J. Smalley, C. W. Ross, J. S. Whitton, Clays from New Zealand support the inactive particle theory of soil sensitivity. *Nature* **288**, 576–577 (1980).
49. E. J. Gabet, S. M. Mudd, The mobilization of debris flows from shallow landslides. *Geomorphology* **74**, 207–218 (2006).
50. S. T. Nase, W. L. Vargas, A. A. Abatan, J. J. McCarthy, Discrete characterization tools for cohesive granular material. *Powder Technol.* **116**, 214–223 (2001).
51. C. J. Brinker, Y. Lu, A. Sellinger, H. Fan, Evaporation-induced self-assembly: Nanostructures made easy. *Adv. Mater.* **11**, 579–585 (1999).
52. E. Rabani, D. R. Reichman, P. L. Geissler, L. E. Brus, Drying-mediated self-assembly of nanoparticles. *Nature* **426**, 271–274 (2003).
53. H. v. Olphen, *An Introduction to Clay Colloid Chemistry, for Clay Technologists, Geologists, and Soil Scientists* (Wiley, Hoboken, NJ, ed. 2, 1977).
54. Y. Xia, G. M. Whitesides, Soft lithography. *Annu. Rev. Mater. Sci.* **28**, 153–184 (1998).

APPLIED PHYSICAL SCIENCES

Seiphoori et al.